Materials Characterization 209 (2024) 113699

Contents lists available at ScienceDirect

Materials Characterization

journal homepage: www.elsevier.com/locate/matchar

The effect of self-organization during deposition on the segregation behaviour of Au in the Si-Ge-Au nano-multilayer thermoelectric generator system

Szilvia Gulyás [a,d], Gábor L. Katona [a,*], Gábor Csiszár [b,c], János J. Tomán [a], Csaba Cserháti [a], Zoltán Erdélyi [a]

[a] Department of Solid State Physics, Faculty of Science and Technology, University of Debrecen, P.O. Box 400, H-4002 Debrecen, Hungary
[b] Institute of Materials Science, University of Stuttgart, Heisenbergstraße 3, D-70569 Stuttgart, Germany
[c] Biomatics and Applied Artificial Intelligence Institute, John von Neumann Faculty of Informatics, Óbuda University, Bécsi út 96/B, H-1034, Budapest, Hungary
[d] University of Debrecen, Doctoral School of Physics, Debrecen, Hungary

ARTICLE INFO

Keywords:
Thermoelectric SiGeAu
Nucleation and growth
Multilayer thin film
Experiments and computer simulations
Microstructure dependent segregation of Au
Au doping

ABSTRACT

Si-Ge-Au amorphous-nanocrystalline composites are important thermoelectric materials where the Seebeck coefficient and the electrical conductivity may be tuned independently. There are many attempts to improve the thermoelectric properties of Si/Ge systems by the addition of additives like Au. However, the effectiveness of doping and the role of Au is not clear. We report on structural transformations and Au segregation behaviour in post-annealed sputter deposited multilayer thin films using composition depth profiling, electron microscopy, x-ray diffraction and computer simulation. We show that depending on the nominal thickness of the initial Au layers the film volume becomes depleted of Au for thinner Au layers while for thicker Au layers the Au content is much higher in the form of large precipitates. Due to the self-organization and changing of microstructure during deposition the segregation of Au is very different for different Au individual layer thicknesses. In case of thinner Au layers it is enriched at the free surface, while for thicker initial Au layer thickness gold accumulated at the substrate. We have carried out computer simulations based on stochastic kinetic mean-field model. These calculations support the argument that initial Au island size can drastically affect the dissolution/growth and segregation behaviour of gold which can significantly influence the thermoelectric parameters. Based on these results we provide a possible explanation to the difference in thermoelectric properties found in the literature.

1. Introduction

Utilizing waste energy is becoming increasingly important nowadays. The application of thermoelectric generators is a possible solution for this problem, however the figure of merit (ZT) values of thermoelectric materials, which characterize the conversion efficiency, still need improvement. Currently, ZT values of somewhat above 2 can be achieved [1,2] in certain materials, but for more widespread application, a wider range of materials together with the further increase of ZT values are needed. A well-known thermoelectric material for high-temperature applications is the Si—Ge system [3]. Within the Si—Ge family of materials, Au doped SiGe is especially promising according to recent results.

Okamoto et al. have found that annealed Si-Ge-Au films show high Seebeck coefficients [4]. They have fabricated artificial superlattice structures to enhance the thermoelectric properties, however the annealed samples showed better thermoelectric parameters despite the transformation of the superlattice structure [5]. Formation of SiGe nanocrystals during the annealing of Si/AuGe artificial superlattice was reported by Takiguchi et al. together with high thermoelectric power [6]. It was speculated that the origin of the high Seebeck coefficient is therefore not the superlattice structure, but the nanocrystals formed during annealing acting as quantum dots. Nevertheless, the high thermoelectric power has low reproducibility, and this assumption has not been verified experimentally.

Large Seebeck coefficients were also reported in annealed Si-Ge-Au films which contained amorphous phase together with nanocrystals [7,8]. Utilizing phonon scattering by nanostructures to effectively lower

* Corresponding author.
E-mail address: gabor.katona@science.unideb.hu (G.L. Katona).

https://doi.org/10.1016/j.matchar.2024.113699
Received 21 August 2023; Received in revised form 18 December 2023; Accepted 23 January 2024
Available online 28 January 2024

thermal conductivity (κ) and thus to increase ZT have been reported several times [9–13]. Introducing nanograins in the amorphous phase resulted in a very low thermal conductivity in the Si-Ge-Au system [14].

Nishino et al. recently studied nanograined Si-Ge-Au thin films fabricated by Molecular Beam Deposition [15]. They annealed multilayer samples under nitrogen atmosphere between 300 and 500 °C for 15–30 min. Formation of SiGe and Au nanocrystals in the amorphous matrix was observed with very low thermal conductivity but without large Seebeck coefficient.

Recently, Sakane et al. proposed a method for the enhancement of the thermoelectric power factor by simultaneous increase of the Seebeck coefficient (S) and the electrical conductivity (σ) [16,17]. They have introduced Au crystals and impurities into SiGe. They claim that they have achieved the highest power factor ($S^2\sigma$) ever reported for SiGe material [17].

It was also shown that the amount of Au changes the grain size of the crystallized SiGe, which in turn affects thermoelectric properties [7,15]. Au also supposed to provide suitable new energy levels near the Fermi level to control the electronic structure in a favourable way [18].

Although, as it can be seen, Si-Ge-Au films are investigated thoroughly in the past decades, their transformations during annealing still have several open questions, especially regarding the formation of Au nanograins and the distribution of Au atoms. A possible reason for this must be the difference in the distribution of additives because of different techniques, initial sample structures, heat treatments, etc.

In this paper, we study the structural transformations in magnetron sputtered Si-Ge-Au multilayers during shorter and also longer annealings. For characterization we utilize depth profiling, X-ray diffraction and transmission electron microscopy. We have also carried out computer simulations to understand the experimental findings better. Our aim is to reveal how the deposition thickness affects the distribution of gold in the Si-Ge-Au system.

2. Experimental

Multilayered SiO_2/{Si/Ge/Au/Ge} × N samples were fabricated on thermally grown Si/SiO_2(100 nm) substrates using DC magnetron sputtering at room temperature. Four sets of samples have been prepared with nominal structures (Fig. 1):

$$S1 : SiO_2/\{Si(6\ nm)/Ge(3.5\ nm)/Au(0.75\ nm)/Ge(3.5\ nm)\} \times 10$$

$$S2 : SiO_2/\{Si(3\ nm)/Ge(1.75\ nm)/Au(0.5\ nm)/Ge(1.75\ nm)\} \times 20$$

$$S3 : SiO_2/\{Si(6\ nm)/Ge(3.5\ nm)/Au(0.5\ nm)/Ge(3.5\ nm)\} \times 10$$

$$S4 : SiO_2/\{Si(3\ nm)/Ge(1.75\ nm)/Au(0.75\ nm)/Ge(1.75\ nm)\} \times 20$$

The amount and ratio of Si and Ge are the same for all samples, only the thicknesses of the individual layers are halved for S2 and S4 together with the doubling of the multilayer repetition. The thicknesses of the Au layers are decreased to 0.5 nm for samples S2 and S4.

Elemental Si, Ge and Au targets were used as sources. The base pressure of the sputtering chamber was 3×10^{-5} Pa, while the pressure of the Ar process gas was 5×10^{-1} Pa. The nominal thicknesses of the layers were calculated from the sputtering time, the deposition rates were 0.075 nm/s for Si, 0.26 nm/s for Ge and 0.12 nm/s for Au.

The as-received samples were annealed in vacuum ($p = 8 \times 10^{-5}$ Pa) at 440 °C for various times. The heating rate was approx. 20 °C/min, while the cooling was not controlled, typical cooling rates were approx. 15 °C/min for the first 150 °C temperature drop. The different annealing times are not parts of an annealing sequence of the same sample, but a separate as-deposited sample was used for each heat-treatment.

The samples were analysed by X-ray diffraction (XRD) using Bragg-Brentano (Θ-2Θ) geometry with Cu-Kα radiation.

Composition depth profiles were obtained using secondary neutral mass spectrometry (SNMS) using a SPECS INA-X SNMS device in direct bombardment mode. Ar plasma was produced to serve as the source of bombarding Ar^+ ions and also as a post-ionization medium. The investigated (sputtered) area of the sample was 3 mm in diameter and high-frequency 350 V bias voltage was applied for sputtering. The intensity-composition conversion was done assuming linear dependence of intensities on concentration.

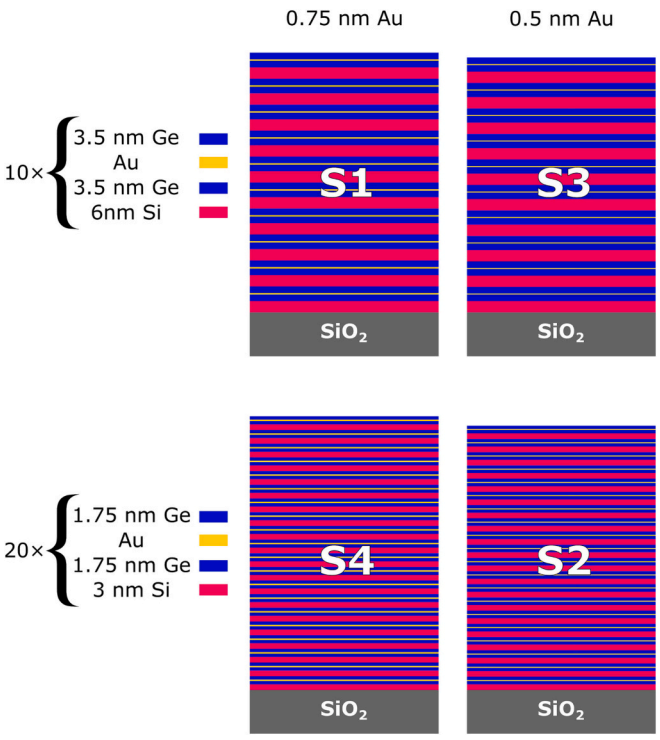

Fig. 1. Visualisation of the samples.

Cross-sections of selected samples were investigated by transmission electron microscopy (TEM), high-resolution transmission electron microscopy (HR-TEM) and scanning electron microscopy in transmission mode (TSEM) to reveal their microstructure.

3. Results

3.1. Sample S1, Thicker Individual Layers

In Fig. 2, SNMS depth profiles are presented for SiO_2/{Si(6)/Ge(3.5)/Au(0.75)/Ge(3.5)} × 10 (S1) samples. Fig. 2a shows the depth profile of the as-deposited sample, showing a clear multilayer structure. The corresponding XRD pattern is shown at the bottom of Fig. 3. As expected, the as-deposited sample shows an amorphous structure.

Annealing at 440 °C for 0.5 h results in the appearance of SiGe reflections indicating crystallization of the amorphous structure (Fig. 3), while in the composition profiles, the multilayer structure is still resolved throughout the whole thickness of the sample (Fig. 2b).

After 4 h at 440 °C, mixing of the individual layers (Fig. 2d) can be seen from the depth profile, but the measurement still shows some signs of the original multilayer structure. From the change of the XRD patterns, further crystallization is apparent (Fig. 3) as the SiGe reflections became stronger along with the appearance of a pronounced Au(111) reflection. Additionally, a peak around 40.8° appears, which is identified as reflection from AuGe.

Annealing for 72 h at 440 °C results in enhanced mixing with still some traces of the original structure as can be seen from the depth profile (Fig. 2e). In the composition profile of Au, an enrichment tendency at the sample/substrate interface becomes very pronounced after

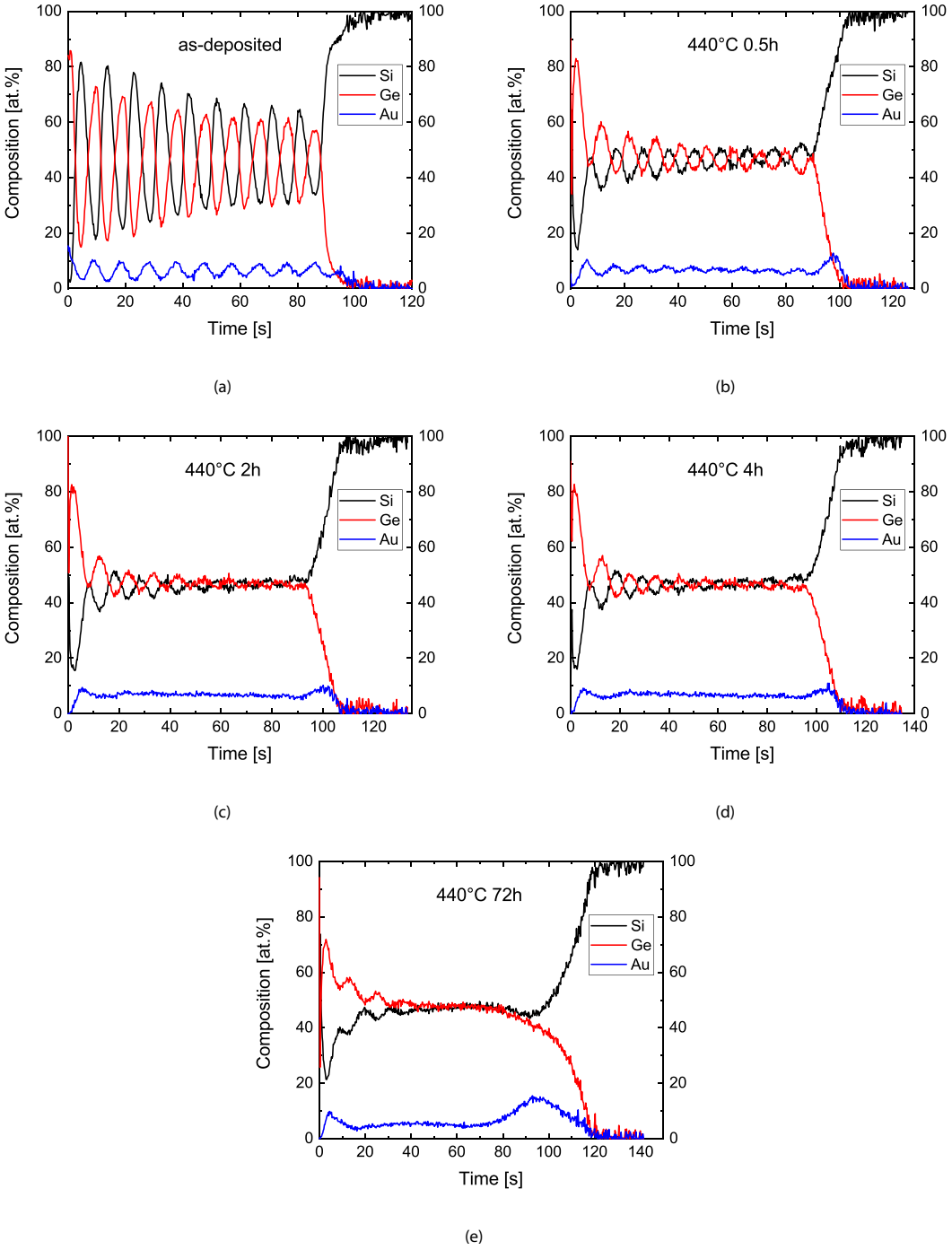

Fig. 2. Depth profiles of the SiO_2/{Si(6)/Ge(3.5)/Au(0.75)/Ge(3.5)} × 10 (S1) samples after various annealing times.

72 h, though some early signs of this were already visible in the shorter heat-treatments, too. The segregation of Au to the free surface is considerably weaker, but clearly present, too. The XRD pattern shows the decrease of the AuGe reflection (Fig. 3), but otherwise no other significant change can be seen.

The sample annealed at 440 °C for 72 h was also investigated by HR-TEM (Fig. 4). The initial layered structure was hardly visible using only HR-TEM. Images made by using TEM/HR-TEM indicate a typical crystalline phase dominating the whole atomic structure. Neither the TEM overview, nor the HR-TEM images can highlight the layered structure after the exposure to 72 h annealing treatment at 440 °C. Electron diffraction patterns confirmed the presence of SiGe phase.

We have also analysed the sample with EDX (energy dispersive X-ray spectroscopy). Typical concentration profiles, together with the corresponding STEM (scanning transmission electron microscopy) HAADF (high-angle annular dark field) images, can be seen in Fig. 5. A residual periodicity from the original layered structure can still be observed as it was also suggested by the SNMS depth profile.

Furthermore, pronounced Au accumulations (light regions) are visible both at the free surface and at the substrate together with large Au precipitations in the volume of the film. The precipitates do not form continuous layers at the interfaces, there are regions practically free from Au. Comparing these local composition profiles with the SNMS depth profiles, one should keep in mind that the SNMS gives an average composition over an area of 3 mm in diameter, so the two methods complement each other very well.

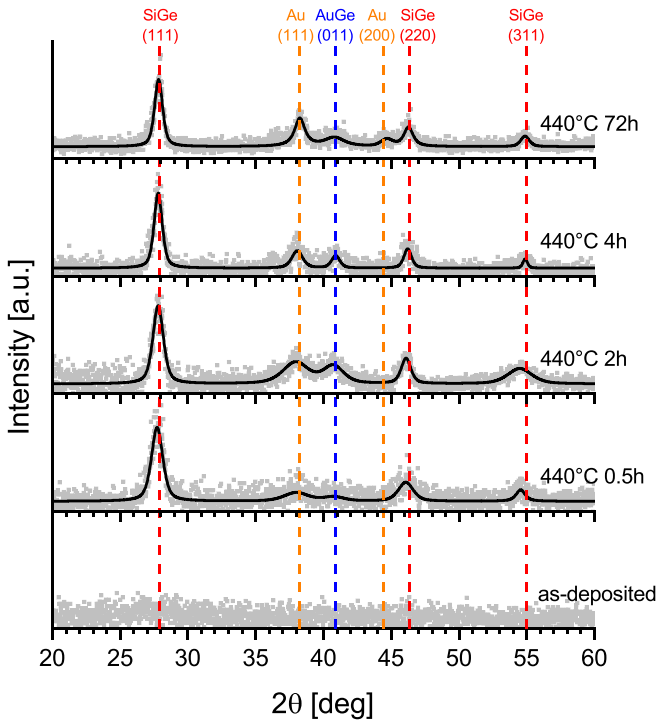

Fig. 3. XRD patterns of the SiO_2/{Si(6)/Ge(3.5)/Au(0.75)/Ge(3.5)} × 10 (S1) samples for various annealing steps.

3.2. Sample S2, Thinner Individual Layers

In case of the sample with thinner individual layers (SiO_2/{Si(3)/Ge(1.75)/Au(0.5)/Ge(1.75)} ×x 20) (S2), the as-deposited depth profile (Fig. 6a) shows the multilayer structure, however the Au layers are hardly resolved due to the very small nominal layer thickness. The XRD pattern (Fig. 7) again proves an amorphous structure. The annealing series is the same as in the previous case, as the S1 and S2 samples were annealed together. After 0.5 h at 440 °C, the original structure is no longer visible in the depth profile (Fig. 6b). The corresponding XRD pattern (Fig. 7 440 °C 0.5 h) shows crystallization with the formation of the same phases (SiGe, Au and AuGe) as in the previous case. However, compared to the first sample (S1), the reflections are more intense, as the XRD pattern is closer to the pattern of the S1 sample annealed for 4 h (Fig. 3 440 °C 4 h). Longer annealing times (Fig. 6d, e) result in more intense Au enrichment and aggregation at the free surface accompanied with slight accumulation of Au at the substrate. The volume of the film has close to homogeneous Si and Ge distribution, even after 0.5 h at 440 °C and the homogeneity further increases after longer annealing. Comparing the final elemental distributions of the two types of samples, it can be seen that the amounts of the segregated and aggregated Au, its preferred interfaces and also the remaining Au contents in the bulks of the films are different in the two cases. The two samples have different average Au contents (~6.8 at.% in the case of S1 vs. ~8.8 at.% in the case of S2), but this cannot explain the differences by itself, since the overall Au content is higher in the thinner layered sample (S2), where the bulk of the film is depleted of Au after annealing.

Examining the XRD patterns (Fig. 7) reveals that despite the fast homogenization of the sample, as seen in the average depth profile, the structural transformation is not finished at the second annealing step (2 h at 440 °C). After 4 h at 440 °C, the SiGe (111) reflection dominates the pattern and reflections from Au can also be seen. Annealing for 72 h at 440 °C results in somewhat sharper peaks together with the increase and sharpening of Au (111) and (200) reflections, indicating the formation of larger, more coherent Au grains.

These samples were also investigated by HR-TEM (Fig. 8). The initial, layered structure, even after the shorter annealing (2 h at 440 °C), is hardly visible by using only (HR)-TEM. The crystalline phase dominates the whole atomic structure and a large number of precipitates have accumulated close to the SiO_2 substrate. Typical EDX concentration profiles together with the corresponding STEM HAADF image can be seen in Fig. 9. The HAADF images (in complete agreement with the SNMS composition profiles) show intensive Au enrichment at the free surface and to a much smaller degree at the substrate. The segregated Au at the surface is not fully continuous; however, there are only smaller discontinuities. In contrast, at the substrate the aggregated amount of Au is much less and there is no similarly continuous layer, only individual precipitates can be seen. There are only a few small Au precipitates in the volume of the film, which is in strong contrast to the thicker layered film (S1) (see Fig. 5), where big Au grains were found. The Si and Ge signals show a close to homogeneous distribution, the original structure is not visible, only some hint can be seen in Fig. 9. These findings are all in very good agreement with the average depth profiles seen from the SNMS measurements (Fig. 6).

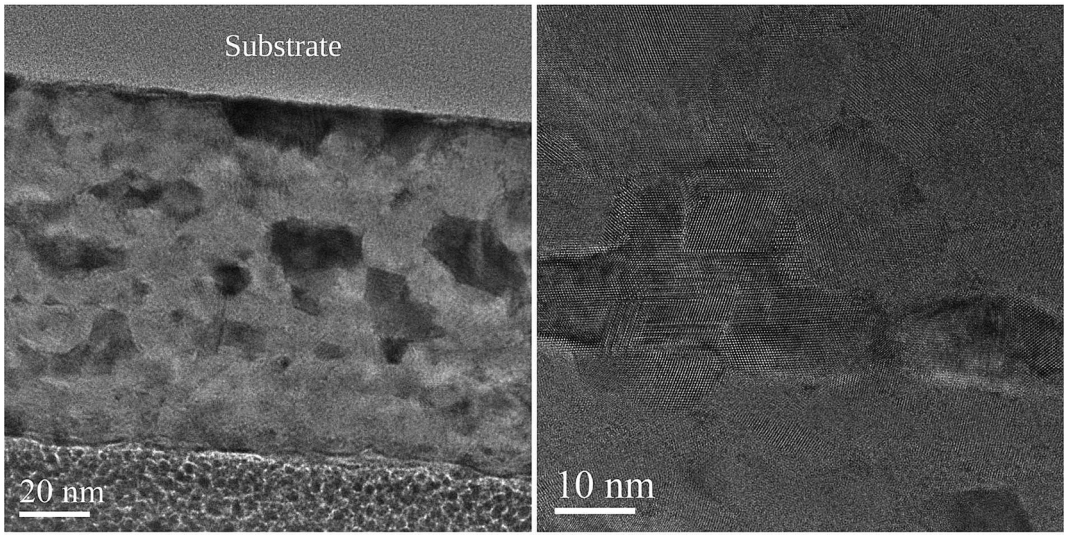

Fig. 4. Bright-field (BF) cross-sectional transmission electron microscopy (TEM) overview images of SiO_2/{Si(6)/Ge(3.5)/Au(0.75)/Ge(3.5)} × 10 (S1) sample annealed at 440 °C for 72 h. The right image shows that crystalline phases dominate the sample which correspond mostly to SiGe alloys.

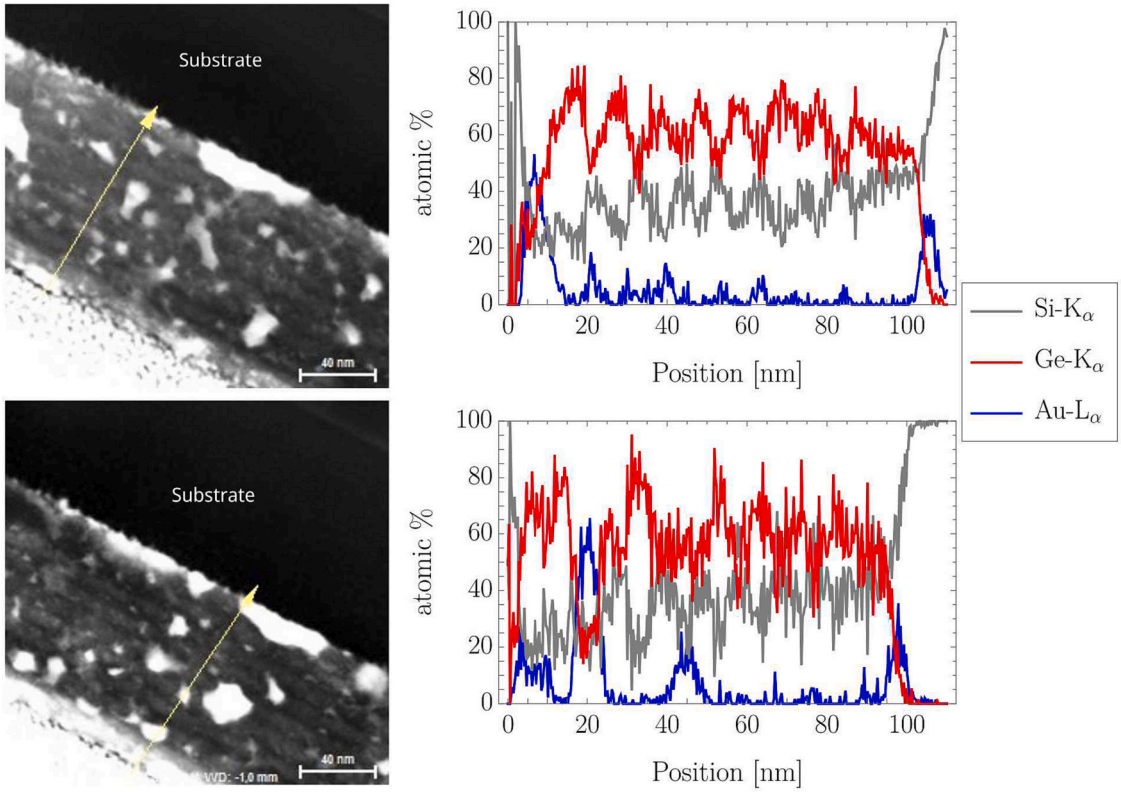

Fig. 5. HAADF image and local EDX analysis of the SiO_2/{Si(6)/Ge(3.5)/Au(0.75)/Ge(3.5)} × 10 (S1) sample annealed at 440 °C for 72 h. The analysis was made in cross-sectional view parallel to the thin film growth direction. The bright parts correspond to Au precipitations.

4. Discussion

For both the S1 and S2 samples, the final states are more or less homogeneously mixed films, in case of sample S1 with still visible traces of the original structures. However, there are major differences between the two sets of samples. In case of the set of samples with thicker individual layers (S1), the majority of Au remains in the volume of the film resulting in high average Au composition. Contrary to this, in the samples with thinner individual layers (S2), the Au content in the volume of the film becomes low, despite the fact that the overall Au content is even higher in this sample. Additionally, there are also differences in the segregation behaviour of Au. In case of the thicker layered samples (S1), the segregation is less pronounced, and it happens primarily to the substrate rather than to the free surface of the sample. In case of the samples with thinner individual layers (S2), the interface enrichment of Au is very pronounced, and it happens primarily to the free surface rather than to the substrate-sample interface.

As we could see in the HR-TEM images, in case of the thicker layered samples (S1), the inner region of the film contains a substantial amount of Au in the form of precipitates. These gold nanocrystals produce the elevated Au content of the bulk of the sample in the SNMS depth profiles, since this technique shows a laterally averaged composition. In case of the thinner layered samples (S2), the HR-TEM images show much smaller Au precipitates, responsible for the lower average Au content in the depth profiles, while the enriched region at the free surface is much thicker and more continuous, despite the shorter annealing time (2 h for the thinner case vs. 72 h for the thicker case).

In order to check the effect of the thickness of the Au layer on the nucleation and growth of Au particles and the segregation tendencies of Au, we have interchanged the Au layer thicknesses between the samples, thus we have created the two other samples (S3 and S4) with the following structures (paired with the S1 and S2 structures):

$$\text{S1}: SiO_2/\{Si(6\text{ nm})/Ge(3.5\text{ nm})/\mathbf{Au(0.75\text{ nm})}/Ge(3.5\text{ nm})\} \times 10$$

$$\mathbf{S3}: SiO_2/\{Si(6\text{ nm})/Ge(3.5\text{ nm})/\mathbf{Au(0.5\text{ nm})}/Ge(3.5\text{ nm})\} \times 10$$

$$\text{S2}: SiO_2/\{Si(3\text{ nm})/Ge(1.75\text{ nm})/\mathbf{Au(0.5\text{ nm})}/Ge(1.75\text{ nm})\} \times 20$$

$$\mathbf{S4}: SiO_2/\{Si(3\text{ nm})/Ge(1.75\text{ nm})/\mathbf{Au(0.75\text{ nm})}/Ge(1.75\text{ nm})\} \times 20$$

In the S3 sample, the Si and Ge layers are thick, but the Au layers were made thinner, like in S2. In the S4 sample, the Si and Ge layers are thin, but the Au layers were made thicker, like in S1; i.e. the thicknesses of Au layers were interchanged between the original S1 and S2 samples.

Fig. 10 shows the SNMS depth profile of the SiO_2/{Si(3)/Ge(1.75)/Au(0.75)/Ge(1.75)} × 20 (S4) sample annealed at 440 °C for 2 h. This is the same annealing as in the case of thinner Au layers with the same Si and Ge layer thicknesses (S2). It can be seen that by increasing the thicknesses of the Au layers, the system now behaves differently. It is now similar to the original thicker layered sample (having the same Au thickness, Fig. 2e) instead of the sample having the same Si and Ge thicknesses (S2) (Fig. 6c); i.e. the bulk of the film has high Au content and the segregation is less pronounced, furthermore, the gold accumulation is significantly stronger to the substrate/sample interface. The thicker Au layer resulted in an interface enrichment behaviour that is more similar to the sample with the same gold layer thickness (S1) than to the sample with same Si and Ge thicknesses but thinner Au.

We have made FIB (focused ion beam)-TSEM images of the S4 sample shown in Fig. 11. The cross-section shows several bigger Au precipitates, which closely resembles the cross-section images of the original thicker layered samples (S1) (Fig. 5). The XRD patterns (not shown) of the samples show the same phases as already described in the sec: Results section.

In case of the SiO_2/{Si(6)/Ge(3.5)/Au(0.5)/Ge(3.5)} × 10 (S3) sample (sample with thicker Si and Ge layers but now with thinner Au),

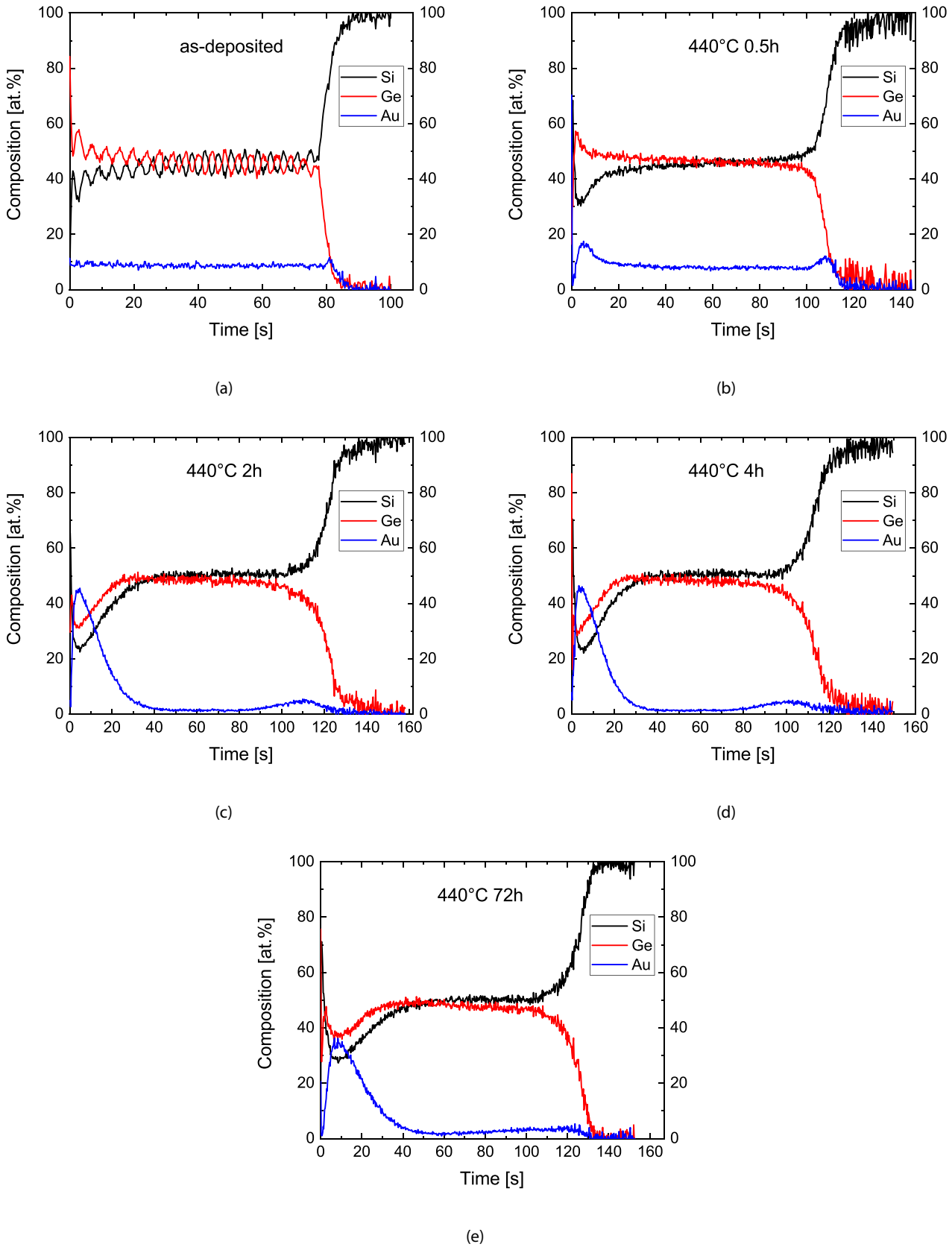

Fig. 6. Depth profiles of the SiO_2/{Si(3)/Ge(1.75)/Au(0.5)/Ge(1.75)} × 20 (S2) samples for various annealing times.

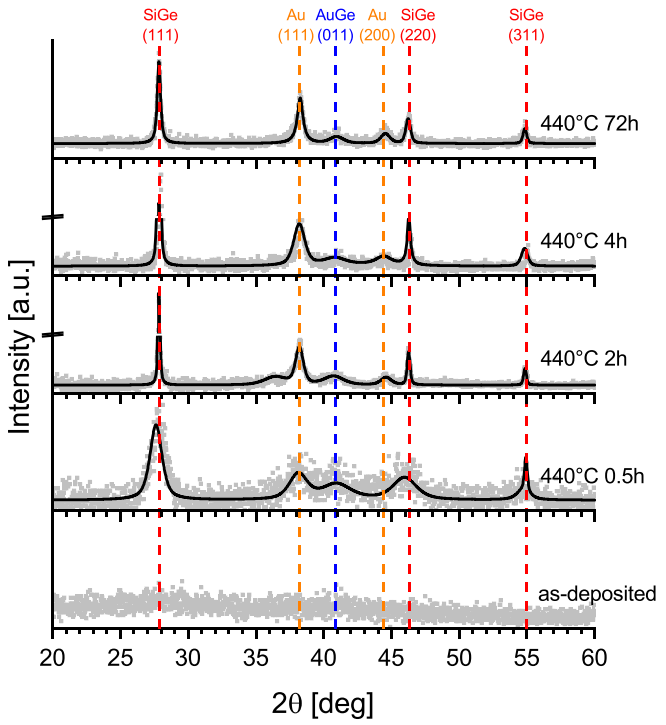

Fig. 7. XRD patterns of the SiO_2/{Si(3)/Ge(1.75)/Au(0.5)/Ge(1.75)} × 20 (S2) samples for various annealing steps.

the SNMS depth profile after annealing at 440 °C for 72 h (Fig. 12) shows that the film volume is depleted of Au, which is heavily aggregated at the free surface. Comparing the behaviour of this sample to S1 and S2, one can see that the new sample's segregation tendency is much closer to the original thinner layered sample with the same Au layer thickness (S2, Fig. 6e) than to S1 with the same Si and Ge thicknesses but with thicker Au layers (Fig. 2e).

We have performed FIB-TSEM investigation on this sample, too (Fig. 13). As it can be seen, the bulk of the film has much smaller Au precipitates as compared to the original thicker layered sample (S1) (Fig. 5) and also compared to the previous modified sample (Fig. 11). The cross-section image resembles of the cross-section of the original thinner layered sample (Fig. 9) where there were also only a small amount of precipitated Au in the volume and enrichment dominantly at the free surface.

Summarizing the results (Fig. 14), it is easy to get to the conclusion that the main determining factor in the segregation behaviour of Au is its nominal layer thickness at deposition. It is not clear, though, why.

To understand this behaviour, we must look closer at what happens during the deposition of the multilayers. In Fig. 15, the cross-section TEM images of the original as-deposited samples S1 and S2 are shown. In these images, we can see how the multilayers change their structure during growth. The first few deposited layers are more or less continuous and planar, although it is clear that moving further away from the substrate, significant changes occur in both samples. One can observe a kind of self-organizing process during deposition. Once the gold layer becomes discontinuous, in the following layers prepared on top of it, the gold is more likely to collect to places above the previous layer's gold islands. This forms patterns or "bands" that are perpendicular to the substrate. A very similar behaviour has been demonstrated in Si—Ge heterostructures [19], where the Ge quantum dots also formed chains in the multilayer. This system is significantly more complicated, though, as Au forms an eutectic system both with Si and Ge.

It can be seen in Fig. 15 that in case of the S1 sample (left), already during deposition, large Au islands form in the volume of the sample. These will become a sink for the atoms coming from the dissolving smaller Au islands. So while the smallest Au islands dissolve, these occasionally scattered large particles in the sample grow even larger keeping the gold in the volume of the thin film. The other large sink for the Au atoms are the layers that were continuous at the beginning, in close proximity of the substrate. From these will form the segregates on the substrate/sample interface.

In case of the S2 sample (right), already the first few Au layers are showing signs of discontinuity, as the layers are made of mostly really small Au islands. A very similar self-organizing behaviour can be seen in this sample, too, as there are bands in the sample that are perpendicular to the surface of the substrate and they lack Au islands. Furthermore, the Au islands are very small in the whole volume of the sample and getting further from the substrate the Si and Ge layers are also becoming discontinuous. Moreover, the Si and Ge layers become indistinguishable forming a mixture already during deposition, which will clearly affect the diffusion of Au.

One of the main variables between the two samples are the sizes of the initial gold islands and their variation with the distance from the substrate surface. Comparing these results, the behaviour of the Au in the original samples can be understood. The Au layers are non-

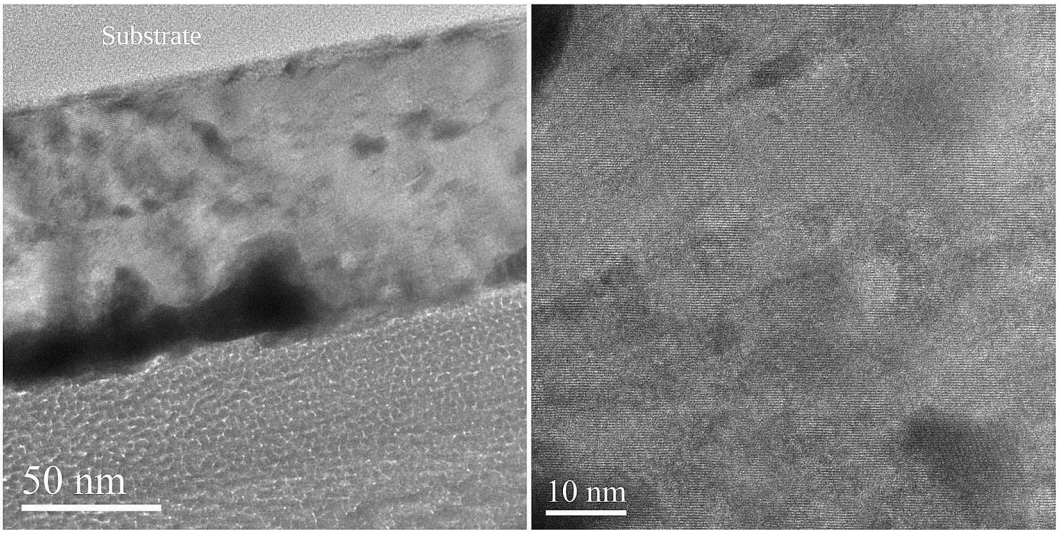

Fig. 8. BF-TEM images of the SiO_2/{Si(3)/Ge(1.75)/Au(0.5)/Ge(1.75)} × 20 (S2) multi-layered thin film exposed to 2 h annealing treatment at 440 °C. The right image shows that crystalline phases dominate the sample.

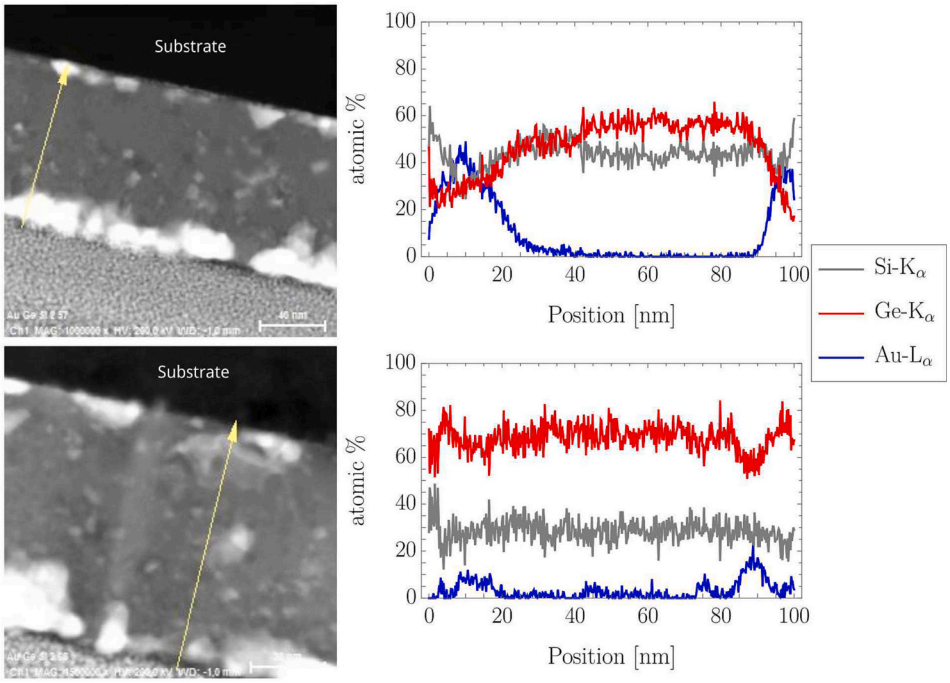

Fig. 9. HAADF image and local EDX analysis of the SiO_2/{Si(3)/Ge(1.75)/Au(0.5)/Ge(1.75)} × 20 (S2) sample annealed at 440 °C for 2 h. The analysis was made in cross-sectional view parallel to the thin film growth direction. The bright parts correspond to Au precipitations.

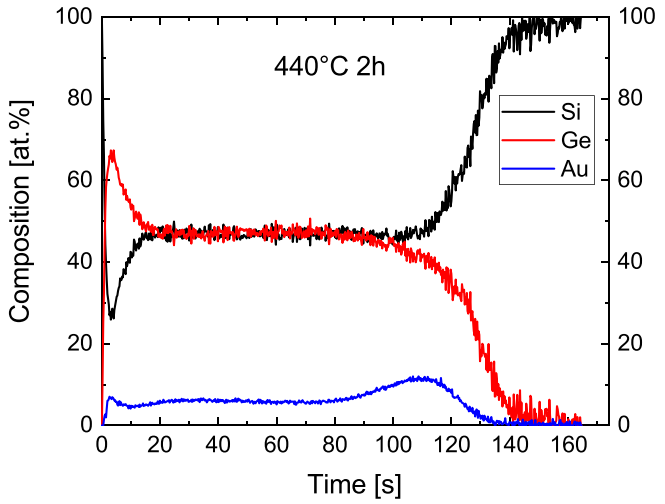

Fig. 10. Depth profile of SiO_2/{Si(3)/Ge(1.75)/Au(0.75)/Ge(1.75)} × 20 (S4) sample annealed at 440 °C for 2 h. Compare it with S1 (Fig. 2e) and S2 (Fig. 6c) samples, see also text. The thicker Au layer resulted in a surface/interface enrichment behaviour that is more similar to the sample with the same Au layer thickness (S1) rather to the sample with the same Si and Ge thicknesses (S2).

continuous as it was confirmed by TEM. The non-continuous Au layers form different sized clusters during deposition. Later, these clusters will serve as the source for Au segregation and they can also act as seeds for nanocrystal growth, if their size is above the nucleation limit. In case of the thicker nominal thickness, probability of bigger clusters having size above the nucleation limit is higher, thus we can expect more clusters growing in place. This will result in higher average Au content in the volume of the film. For the thinner nominal Au thickness, the number of seeds capable of growing is significantly lower, thus more Au will be able to segregate, leaving a Au poor film volume with only a few Au grains. This corresponds well to the observed chemical distribution and morphological images.

The reason for the different segregation tendencies is the remaining question. As we could see, in case of the thicker nominal Au layers, annealing at 440 °C results in a segregation tendency to the substrate/sample interface, while the thinner nominal Au layers result in segregation to the free surface. The answer to this phenomenon lies in the self-organization behaviour during deposition.

In samples with the thicker nominal layers, the first few gold layers, close to the substrate will form a large sink of the dissolved Au atoms. The forming large Au nanocrystals will naturally tend to form on the substrate/surface interface as the closest energetically favourable surface. Further away from the substrate, the initial Au islands are already large, so the main processes are not dissolution, but growth and Ostwald ripening, resulting in large Au precipitates in the volume.

In the samples with thinner nominal layers, the Au islands in the as-deposited sample are generally a lot smaller, meaning that growth instead of dissolution is preferable only for a small portion of them. This will result in the dissolution of Au in the vast majority of the sample and after the dissolved gold segregates to one of the interfaces, the volume of the film will maintain a low Au concentration. The gold that is contained in the first few, more or less continuous Au layers will cause some enrichment on the substrate/sample interface, similarly to S1, although to a much lesser extent. Other than that, the largest individual Au islands after deposition are generally very close to the surface of the sample. Furthermore, the changing nanostructure during deposition means that the individual Au, Ge and Si layers are not continuous further away from the substrate, which provides very easy diffusion pathways for the dissolved Au to the free surface. This results in a much stronger enrichment at the free surface in this case.

In addition, it should be mentioned that the annealing temperature is above the eutectic temperatures of both Au—Si and Au—Ge systems [20], thus there can be local liquid parts which can enhance crystallization and grain growth [7,21]. Moreover, it can also serve as the source of mobile particles/droplets [22,23]. For these migrating particles, the free surface serves as a sink which also increases the enrichment and aggregation of Au at the surface.

In order to confirm that the initial Au island size can have a significant effect on the coarsening and segregation tendencies, computer

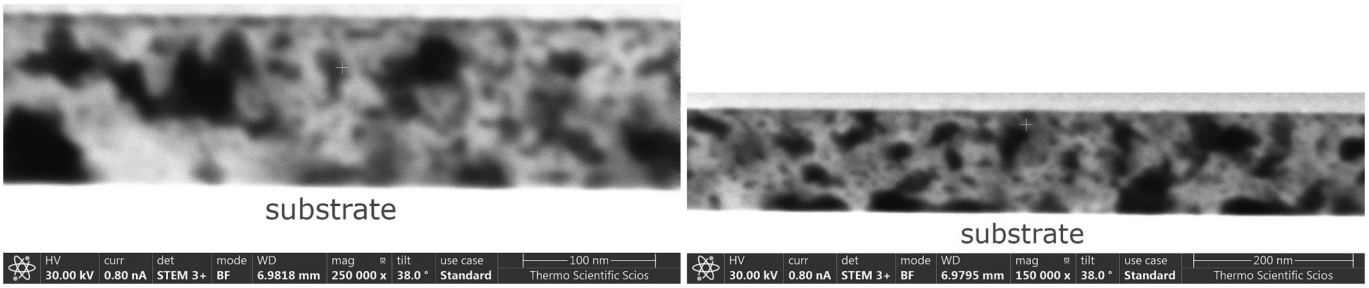

Fig. 11. BF-FIB-TSEM cross-sections of the SiO_2/{Si(3)/Ge(1.75)/Au(0.75)/Ge(1.75)} × 20 (S4) sample annealed for 2 h at 440 °C. The dark parts correspond to Au precipitations.

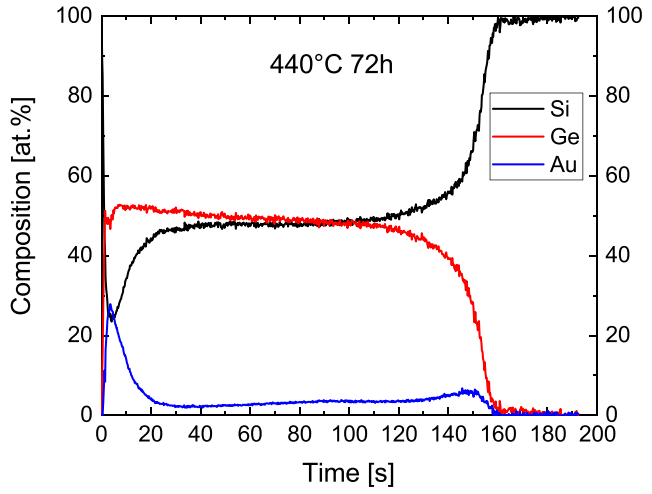

Fig. 12. Depth profile of SiO_2/{Si(6)/Ge(3.5)/Au(0.5)/Ge(3.5)} × 10 (S3) sample annealed at 440 °C for 72 h. Compare it with S1 (Fig. 2e) and S2 (Fig. 6e) samples, see also text. The thinner Au layer resulted in a surface/interface enrichment behaviour that is more similar to the sample with the same Au layer thickness (S2) rather to the sample with the same Si and Ge thicknesses (S1).

simulations were designed. The computer model used is an improved version of the original SKMF (stochastic kinetic mean-field) [24] model which includes some of the ideas from 3DO-SKMF (3D-object stochastic kinetic modelling framework) [25,26]. Similarly to the original SKMF model, the system has periodic boundary conditions in x and y directions, but vertically the system is finite. From above, it is bounded by an environment (E) and from below, it is connected to a substrate (S). As we see from this work, these interfaces can be very important from application point of view. The detailed description of the model can be found in Appendix A.

In our calculations, we have chosen a regular solution parameter $V = 0.4kT$ (k is the Boltzmann-constant and T is the absolute temperature), which means that the solubility of Au in the SiGe matrix is $c_{eq} \approx 0.89$ at. % and vice versa. To control the segregation to both of the interfaces, $\sigma_E = \sigma_S = -0.16kT$ was chosen which means that the segregation of gold is energetically favourable in the system, but it happens in islands first, without fully covering the interface, as it can be seen in the experimental samples. The effects of changing the values of the σ parameters on the segregation tendencies have been demonstrated in ref. [26].

In the simulations, the gold is initially distributed in separate layers as non-overlapping hemispherical particles. The shape of the particles are an estimate to the islands that form during deposition as they are assumed to grow on a flat surface. The radiuses of the particles follow the Irwin-Hall distribution [27] as an approximation to normal distribution. The same amount of Au is used in the two cases. Although the numbers of the particles (and consequently their sizes) are different in the two initial states. The characteristic average lateral distance is 2.5 times larger in the first case. In practice, this means that in the sections shown in Fig. 16, the same amount of Au in the same surface area is distributed in 4 and 25 particles.

In Fig. 16, we show the initial states of the simulations and snapshots after the same length of heat-treatment. The amount of material segregated to the free surface and the sample/substrate interface, hence also the amount of Au remaining in the volume of the film, depends strongly on the initial size distribution of the gold particles. This suggests that the different size-distributions of the gold islands, due to the different nominal thicknesses of the sputtered gold layers, can indeed play important roles in the different segregation behaviours observed in the experiments.

In previous works, it became clear that the amount of Au and Au precipitations in the crystallized Si—Ge composite is an important factor determining the thermoelectric properties.

In case of annealed multilayer Si/Ge/Au thin film samples [15] no increased value of $S^2\sigma$ and power factor was found, although the samples showed very low thermal conductivity. The authors claimed that the samples were prepared similarly to previous studies [7] where increased power factor was detected. It was assumed, based on these works, that Au is precipitated in the volume of the annealed film,

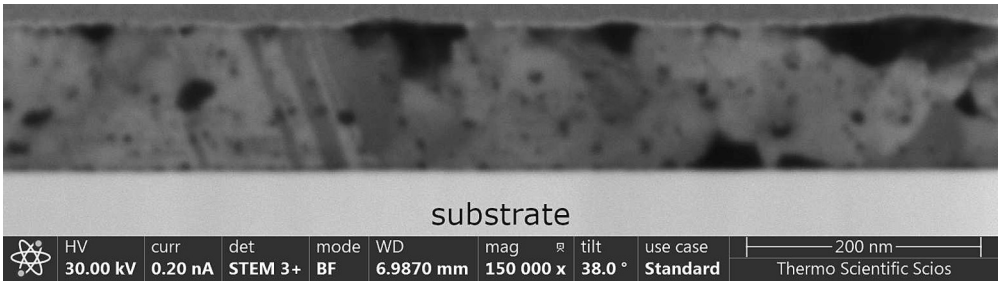

Fig. 13. BF-FIB-TSEM cross-section of the SiO_2/{Si(6)/Ge(3.5)/Au(0.5)/Ge(3.5)} × 10 (S3) sample annealed at 440 °C 72 h. The dark parts correspond to Au precipitations.

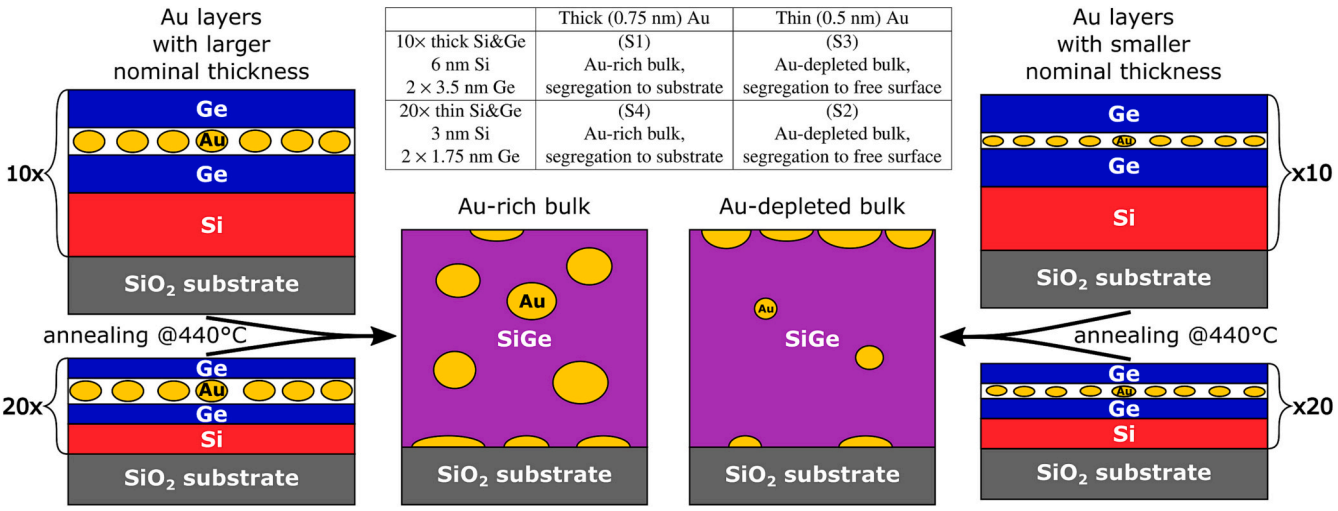

	Thick (0.75 nm) Au	Thin (0.5 nm) Au
10× thick Si&Ge 6 nm Si 2 × 3.5 nm Ge	(S1) Au-rich bulk, segregation to substrate	(S3) Au-depleted bulk, segregation to free surface
20× thin Si&Ge 3 nm Si 2 × 1.75 nm Ge	(S4) Au-rich bulk, segregation to substrate	(S2) Au-depleted bulk, segregation to free surface

Fig. 14. Summary of the experimental findings.

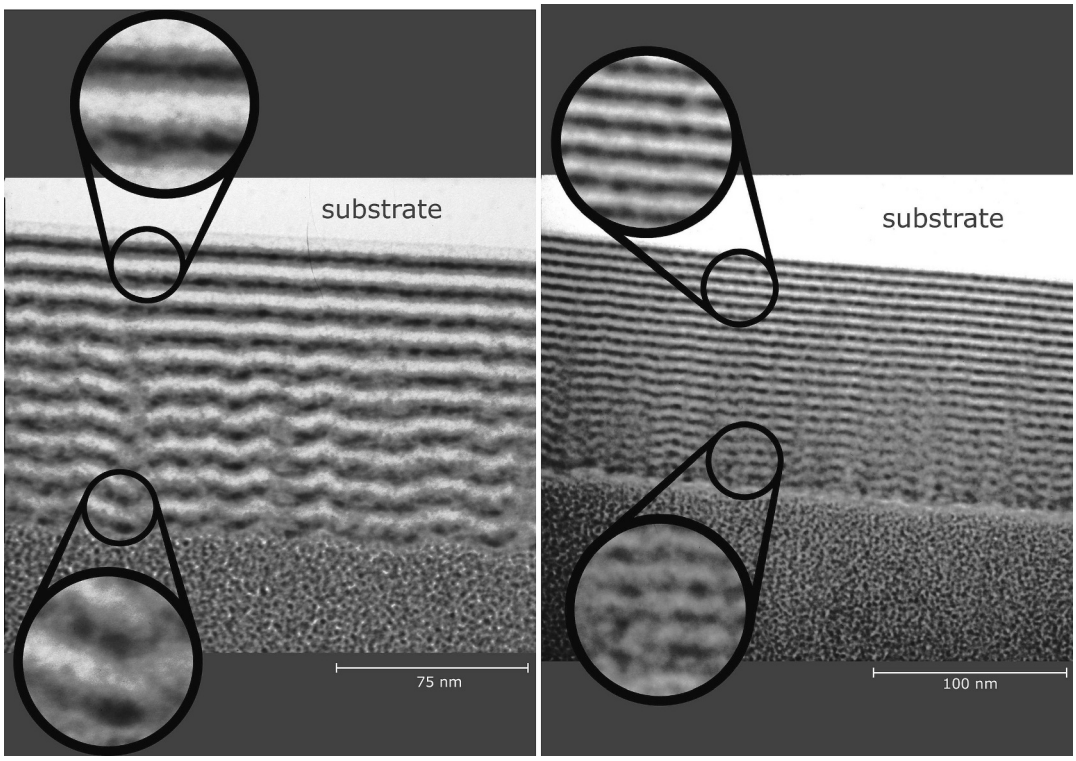

Fig. 15. Cross-section BF-TEM image of samples S1 (left) and S2 (right).

however it was not checked and the nominal initial thickness of the Au layers in the multilayer structure was below 0.4 nm.

In contrast to this, high values of $S^2\sigma$ were recently reported in SiGe-Au nanocomposite materials made by suction casting [16,17]. These samples contained Au precipitations at the grain boundaries in the volume of the sample as proved by SEM images.

Taking into account our experimental and computer simulation results, a possible explanation of the different thermoelectric properties is based on the difference in the distribution of Au. As we have shown, in case of very thin Au layers or very small initial Au precipitations, the volume of the sample tends to be depleted of Au instead of forming precipitations, which will influence the thermoelectric parameters.

5. Conclusion

There are many examples in the literature for attempts to improve the thermoelectric properties of Si/Ge systems by the addition of additives like Au. However, the effectiveness of doping is not clear and sometimes controversial. We suspect that the reason for this is that the distribution of additives introduced by different techniques, in different amounts and in structures that have been often also subjected to heat treatment can vary dramatically. To study this, we investigated Si/Ge/Au/Ge multilayers with four different individual layer thickness combinations after various annealing durations at 440 °C.

1. Rapid crystallization was observed in all samples, which resulted in the formation of mainly SiGe and Au nanocrystalline grains. The

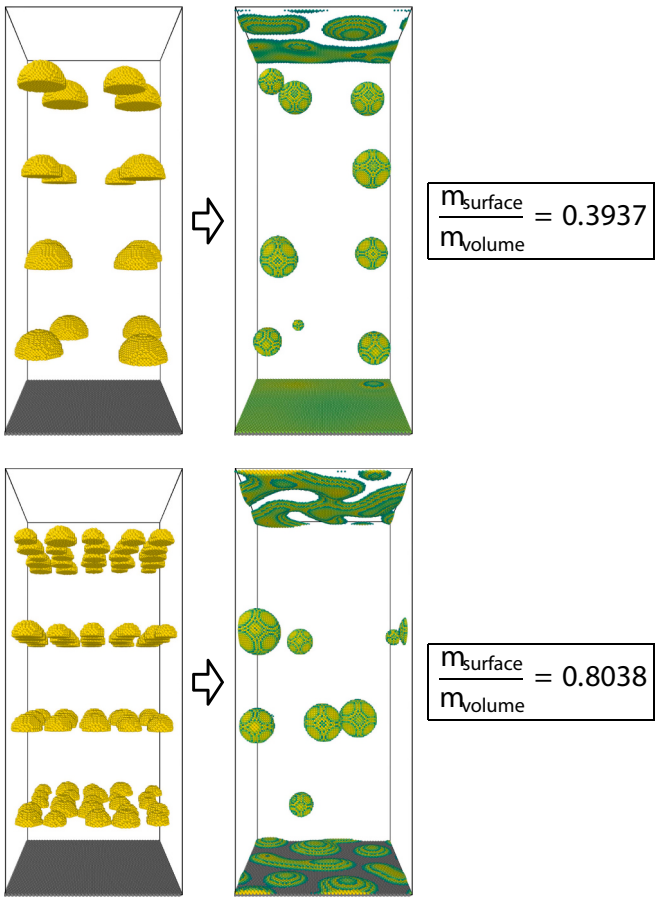

Fig. 16. Simulation results of two systems initially starting with the same amount of gold, but with different spacial distributions. In the first case, the gold is distributed in a lower number of particles with larger radiuses, while in the second case, the gold is in a larger number of smaller particles. The different surface/volume ratios and curvatures of the islands lead to different dissolution kinetics and different amounts of gold segregated to the interfaces with the substrate and the external environment after the same amount of time. Only sites with $c_i > 0.5$ Au occupation probabilities are shown. (For interpretation of the references to colour in this figure legend, the reader is referred to the web version of this article.)

formation of these phases was accompanied with segregation and enrichment of Au at the free surface or at the substrate.

2. Depending on the thicknesses of the Au layers, 0.5 nm or 0.75 nm, the volume of the film was either depleted of Au, having only a few Au grains (in samples with 0.5 nm Au layers) or showed high Au content corresponding to several large Au precipitates (in samples with 0.75 nm Au layers).
3. The experimental findings were interpreted by the different cluster sizes of the initial non-continuous Au layers, having seeds above or below the nucleation limit. Due to the changing microstructure and self-organization during the preparation of the multilayers, the segregation tendencies are also different in the case of the two nominal Au layer thicknesses:

   (a) With the thinner Au layers, the dissolution of Au is accompanied by a strong segregation and aggregation at the free surface.
   (b) With the thicker nominal Au layer thicknesses, the formation of large Au precipitates in the volume of the film is accompanied by gold's segregation to the substrate/sample interface.

4. Computer simulations were used to strengthen the argument that the initial island size can significantly affect the dissolution/growth and segregation behaviour.

Applying our results, we have provided possible explanation to the differences found in previous reports, based on the different distribution of Au in the volume of samples. Our findings emphasize that the described effects should be taken into account when tailoring sample structures and thermal treatments, because the precipitation or segregation of a third component like Au may significantly affect the desired properties.

CRediT authorship contribution statement

Szilvia Gulyás: Investigation, Writing – original draft, Writing – review & editing, Visualization, Formal analysis, Data curation, Software. **Gábor L. Katona:** Conceptualization, Data curation, Methodology, Validation, Writing – original draft, Writing – review & editing, Formal analysis, Supervision, Investigation. **Gábor Csiszár:** Investigation, Data curation, Formal analysis. **János J. Tomán:** Formal analysis, Investigation, Software, Visualization, Writing – original draft, Writing – review & editing. **Csaba Cserháti:** Investigation. **Zoltán Erdélyi:** Conceptualization, Methodology, Writing – original draft, Writing – review & editing, Supervision, Formal analysis, Funding acquisition, Investigation, Software.

Declaration of competing interest

The authors declare that they have no known competing financial interests or personal relationships that could have appeared to influence the work reported in this paper.

Data Availability

Data will be made available on request.

Acknowledgements

The authors thank Mr. P. Kopold for assistance with the (HR)TEM measurements. Project no. TKP2021-NKTA-34 has been implemented with the support provided from the National Research, Development and Innovation Fund of Hungary, financed under the TKP2021-NKTA funding scheme. The authors are grateful for the support of the National Research Development and Innovation Office by the 2019-2.1.11-TÉT-2019-00061 project.

Appendix A. Details of the Computer Model

In the model, we define a fixed three-dimensional lattice, in which c_i occupation probabilities are calculated, which is the probability that site i is occupied by an A atom (in this case this will represent gold). Consequently, in a binary model $1 - c_i$ is the probability of site i being occupied by the B matrix (which will be the Ge—Si mixture here). Similar concept has been published previously [28,29]. We would like to point the reader to works by Gusak et al. [30,31], where the authors compare the two methods. The time evolution of c_i is caused by the flow of occupation probability between site i and its p_i number of nearest neighbouring sites j, naturally obeying to the law of conservation of matter:

$$\frac{dc_i}{dt} = -\sum_{j=1}^{p_i} \left[J_{i,j} - J_{j,i}\right]. \tag{A.1}$$

The J currents are:

$$J_{i,j} = J_{i,j}^{\mathrm{MF}} = c_i\left(1 - c_j\right)\Gamma_{i,j}^{\mathrm{MF}}, \tag{A.2}$$

where $J_{i,j}^{\mathrm{MF}}$ is the current of occupation probability of A from the site i to j and, of course, that of B the other way around (as if component A would flow from i to j and component B vice versa). $\Gamma_{i,j}^{\mathrm{MF}}$ shows the exchange rate of the occupation probability between site i and j in mean-field approximation (similarly to the exchange probability of an A atom on site i and a B atom on site j in a kinetic Monte Carlo by exchange mechanism or by vacancy mechanism with equilibrium vacancy compositions):

$$\Gamma_{i,j}^{\mathrm{MF}} = \nu exp\left(-\frac{2E_0 - \left(E_i^A + E_j^B\right)}{\mathrm{k}T}\right), \tag{A.3}$$

where ν is the frequency of jump attempts, k is the Boltzmann constant, T is the absolute temperature, E_0 is the saddle point energy and $E_i^A + E_j^B$ is the sum of the interaction energies of an A atom on site i and a B atom on site j. The interaction energies are defined as the sums of the pair interaction energies between the atoms on the sites and the neighbouring atoms, weighted by their occupation probabilities. The total interaction energy of an X (A or B) atom on site h (i or j) is therefore:

$$E_h^X = \sum\nolimits_{hn=1}^{p_h} c_{hn} V_{AX} + \sum\nolimits_{hn=1}^{p_h} (1 - c_{hn}) V_{XB} + e_h V_{XE} + s_h V_{XS}, \tag{A.4}$$

where we assume that the first coordination shell of the given site consists of $Z = p_h + e_h + s_h$ sites, where Z is the coordination number of the lattice, p_h is the number of bonds of site h inside the sample, e_h is the number of bonds formed between an atom on site h and the environment, while s_h is the number of bonds formed between the atom on site h and the substrate. For bonds formed within the sample, the probability of a neighbouring hn site being occupied by material A is c_{hn} and consequently the occupation probability for material B is $1 - c_{hn}$. The substrate and the environment both are considered as pure. Furthermore, while there are chemical interactions between them and the A and B materials of the system, no material transfer occurs via these interfaces. V_{AA}, V_{BB} and V_{AB} are the A–A, B–B and A–B pair interaction energies inside the sample, while V_{AS} and V_{BS} are the pair interaction energies between the substrate and A and B materials, respectively. V_{AE} and V_{BE} are defined similarly for the environment.

In this work, we considered only nearest neighbour interactions and phase separation, but the model is not limited to these cases. Further interaction shells and chemical ordering can also be taken into account [31] and even n-body potentials can be considered. Furthermore, due to the continuous nature of the occupation probabilities on the lattice sites, composition dependent interaction energies can also be easily implemented [32] and the method can be conveniently used as the atomic scale member of multi-scale simulations [33].

After some algebra one can find that:

$$\begin{aligned} E_i^A + E_j^B = {} & (M - V)\sum_{in=1}^{p_i} c_{in} + (M + V)\sum_{jn=1}^{p_j} c_{jn} \\ & + 2Z\varepsilon_0 + \frac{1}{2}V\left(p_i - p_j\right) \\ & + \varepsilon_E\left(e_i + e_j\right) + \varepsilon_S\left(s_i + s_j\right) \\ & + \sigma_E\left(e_i - e_j\right) + \sigma_S\left(s_i - s_j\right) \end{aligned} \tag{A.5}$$

Where the sites inside the simulated volume and neighbouring i and j are marked by in and jn subscripts, respectively. (These do not include sites of the environment or substrate.) The parameters in Eq. (A.5) can be estimated from either macroscopic measurements or from ab initio calculations. These are the actual input parameters of the model to describe the system's kinetic and thermodynamic properties:

$$\begin{aligned} M &= \frac{V_{AA} - V_{BB}}{2} \\ V &= V_{AB} - \frac{V_{AA} + V_{BB}}{2} \\ \varepsilon_0 &= \frac{V_{AB} + V_{BB}}{2} \\ \varepsilon_E &= \frac{V_{AE} + V_{BE}}{2} - \varepsilon_0 \\ \varepsilon_S &= \frac{V_{AS} + V_{BS}}{2} - \varepsilon_0 \\ \sigma_E &= \frac{V_{AE} - V_{BE}}{2} - \frac{M}{2} \\ \sigma_S &= \frac{V_{AS} - V_{BS}}{2} - \frac{M}{2}. \end{aligned} \tag{A.6}$$

The ε_E and ε_S parameters determine the jump frequencies along the sample–environment and sample–substrate interfaces, while the σ_E and σ_S parameters determine the segregation tendencies to these interfaces. The thermodynamic behaviour of the bulk system is described by V, that is, it determines the values of the bulk solubilities and spinodal limits independently of the value of M. The M parameter represents the composition dependence of the Brownian diffusion coefficients in the bulk, that is, it affects "only" the kinetic behaviour of the system.

As it was shown in ref. [33], the excess Gibbs energy in the SKMF model with a constant V is equivalent to the one received from the mean-field approximation. Accordingly, the system's phase diagram can be calculated by finding the compositions where the first derivative of the excess Gibbs

energy is zero (these are the solubility limits) and where its second derivative is zero (giving the spinodal limits).

We solve the differential equations in dimensionless form. Energy is measured in kT units, while time is normalized by $[\nu exp\{-2E_0/(kT)\}]^{-1}$.

The reader might have been wondering already, why the name of the model contains the term "stochastic", while no stochastic term is introduced in the formulas. It was shown in ref. [31] that without additionally introduced stochastic noise, the model decreases the free energy of the system in a monotonic way. This is sufficient if there are no energetic barriers in the behaviour of the system, e.g. the barrier for homogeneous nucleation. Considering that the gold have already formed islands during the deposition, introduction of stochasticity is not necessary. If the reader is interested in the stochastic part of the model, multiple publications are discussing it [24,30,34]. Without noise/stochasticity, the model is also useful for calculating equilibrium states, e.g. 3D, radius- and composition-dependent phase diagrams of Janus nanoparticles [35].

References

[1] M. Rull-Bravo, A. Moure, J.F. Fernández, M. Martín-González, Skutterudites as thermoelectric materials: revisited, RSC Adv. 5 (52) (2015) 41653–41667, https://doi.org/10.1039/C5RA03942H.

[2] D. Champier, Thermoelectric generators: a review of applications, Energ. Conver. Manage. 140 (2017) 167–181, https://doi.org/10.1016/j.enconman.2017.02.070.

[3] A. Nozariasbmarz, A. Agarwal, Z.A. Coutant, M.J. Hall, J. Liu, R. Liu, A. Malhotra, P. Norouzzadeh, M.C. Öztürk, V.P. Ramesh, Y. Sargolzaeiaval, F. Suarez, D. Vashaee, Thermoelectric silicides: a review, Jpn. J. Appl. Phys. 56 (5S1) (2017) 05DA04, https://doi.org/10.7567/JJAP.56.05DA04.

[4] Y. Okamoto, H. Uchino, T. Kawahara, J. Morimoto, Anomalous large thermoelectric power of the Si and Au doped Ge superlattice thin film, Jpn. J. Appl. Phys. 38 (1999) L945–L947, https://doi.org/10.1143/JJAP.38.L945 (Part 2, No. 8B).

[5] H. Uchino, Y. Okamoto, T. Kawahara, J. Morimoto, The study of the origin of the anomalously large thermoelectric power of Si/Ge Superlattice thin film, Jpn. J. Appl. Phys. 39 (2000) 1675–1677, https://doi.org/10.1143/JJAP.39.1675 (Part 1, No. 4A).

[6] H. Takiguchi, K. Fukui, Y. Okamoto, Annealing temperature dependence of crystallization process of SiGeAu thin film, Jpn. J. Appl. Phys. 49 (11) (2010) 115602, https://doi.org/10.1143/JJAP.49.115602.

[7] H. Takiguchi, M. Aono, Y. Okamoto, Nano structural and thermoelectric properties of SiGeAu thin films, Jpn. J. Appl. Phys. 50 (4) (2011) 041301, https://doi.org/10.1143/JJAP.50.041301.

[8] M. Hamabe, H. Takahashi, S. Yamaguchi, T. Komine, T. Eura, H. Okumura, Y. Okamoto, J. Morimoto, Thermoelectric characteristics of Si/Ge superlattice thin films at temperatures less than 300 K, Jpn. J. Appl. Phys. 42 (2003) 6779–6783, https://doi.org/10.1143/JJAP.42.6779 (Part 1, No. 11).

[9] X.W. Wang, H. Lee, Y.C. Lan, G.H. Zhu, G. Joshi, D.Z. Wang, J. Yang, A.J. Muto, M. Y. Tang, J. Klatsky, S. Song, M.S. Dresselhaus, G. Chen, Z.F. Ren, Enhanced thermoelectric figure of merit in nanostructured n-type silicon germanium bulk alloy, Appl. Phys. Lett. 93 (19) (2008) 193121, https://doi.org/10.1063/1.3027060.

[10] G. Joshi, H. Lee, Y. Lan, X. Wang, G. Zhu, D. Wang, R.W. Gould, D.C. Cuff, M. Y. Tang, M.S. Dresselhaus, G. Chen, Z. Ren, Enhanced thermoelectric figure-of-merit in nanostructured p-type silicon germanium bulk alloys, Nano Lett. 8 (12) (2008) 4670–4674, https://doi.org/10.1021/nl8026795.

[11] A. Samarelli, L. Ferre Llin, S. Cecchi, J. Frigerio, T. Etzelstorfer, E. Müller, Y. Zhang, J.R. Watling, D. Chrastina, G. Isella, J. Stangl, J.P. Hague, J.M. R. Weaver, P. Dobson, D.J. Paul, The thermoelectric properties of Ge/SiGe modulation doped superlattices, J. Appl. Phys. 113 (23) (2013) 233704, https://doi.org/10.1063/1.4811228.

[12] L. Ferre Llin, A. Samarelli, S. Cecchi, T. Etzelstorfer, E. Müller Gubler, D. Chrastina, G. Isella, J. Stangl, J.M.R. Weaver, P.S. Dobson, D.J. Paul, The cross-plane thermoelectric properties of p-Ge/Si $_{0.5}$ Ge $_{0.5}$ superlattices, Appl. Phys. Lett. 103 (14) (2013) 143507, https://doi.org/10.1063/1.4824100.

[13] S. Yamasaka, K. Watanabe, S. Sakane, S. Takeuchi, A. Sakai, K. Sawano, Y. Nakamura, Independent control of electrical and heat conduction by nanostructure designing for Si-based thermoelectric materials, Sci. Rep. 6 (1) (2016) 22838, https://doi.org/10.1038/srep22838.

[14] Y. Okamoto, J. Saeki, T. Ohtsuki, H. Takiguchi, Thermal conductivity measurement of Si/(Ge+Au) artificial Superlattice thin film, Appl. Phys. Express 1 (2008) 117001, https://doi.org/10.1143/APEX.1.117001.

[15] S. Nishino, S. Ekino, M. Inukai, M. Omprakash, M. Adachi, M. Kiyama, Y. Yamamoto, T. Takeuchi, Thermoelectric properties of Nanograined Si-Ge-Au thin films grown by molecular beam deposition, Journal of Electronic Materials 47 (6) (2018) 3267–3272, https://doi.org/10.1007/s11664-017-5981-z.

[16] S. Sakane, T. Ishibe, K. Mizuta, M. Kashino, K. Watanabe, T. Fujita, Y. Kamakura, N. Mori, Y. Nakamura, Methodology of thermoelectric power factor enhancement by nanoscale thermal management in Bulk SiGe composites, ACS Applied Energy Materials 3 (1) (2020) 1235–1241, https://doi.org/10.1021/acsaem.9b02340.

[17] S. Sakane, T. Ishibe, K. Mizuta, T. Fujita, Y. Kiyofuji, J.-i. Ohe, E. Kobayashi, Y. Nakamura, Anomalous enhancement of thermoelectric power factor by thermal management with resonant level effect, J. Mater. Chem. A 9 (8) (2021) 4851–4857, https://doi.org/10.1039/D0TA08683E.

[18] M. Adachi, S. Nishino, K. Hirose, M. Kiyama, Y. Yamamoto, T. Takeuchi, High dimensionless figure of Merit ZT = 1.38 achieved in p-Type Si–Ge–Au–B thin film, Materials Transactions 61 (5) (2020) 1014–1019, publisher: The Japan Institute of Metals and Materials, https://doi.org/10.2320/matertrans.MT-M2019310.

[19] V.A. Yuryev, L.V. Arapkina, M.S. Storozhevykh, O.V. Uvarov, V.P. Kalinushkin, Dense chains of stacked quantum dots in Ge/Si heterostructures, in: R. Adelung (Ed.), SPIE Proceedings, SPIE, 2013, https://doi.org/10.1117/12.2017072.

[20] T.B. Massalski, H. Okamoto, ASM International (Eds.), Binary Alloy Phase Diagrams, 2nd edition, ASM International, Materials Park, Ohio, 1990.

[21] H. Takiguchi, Z. Yoshikawa, H. Miyazaki, Y. Okamoto, J. Morimoto, The role of Au in the thermoelectric properties of amorphous Ge/Au and Si/Au thin films, J. Electron. Mater. 39 (9) (2010) 1627–1633, https://doi.org/10.1007/s11664-010-1267-4. http://link.springer.com/10.1007/s11664-010-1267-4.

[22] Q. Liu, R. Zou, J. Wu, K. Xu, A. Lu, Y. Bando, D. Golberg, J. Hu, Molten Au/Ge alloy migration in ge nanowires, Nano Lett. 15 (5) (2015) 2809–2816, https://doi.org/10.1021/acs.nanolett.5b01144.

[23] F. Leroy, A. El Barraj, F. Cheynis, P. Müller, S. Curiotto, Atomic transport in au-ge droplets: brownian and electromigration dynamics, Physical Review Letters 123 (17) (2019), https://doi.org/10.1103/PhysRevLett.123.176101.

[24] Z. Erdélyi, M. Pasichnyy, V. Bezpalchuk, J.J. Tomán, B. Gajdics, A.M. Gusak, Stochastic kinetic mean field model, Comput. Phys. Commun. 204 (2016) 31–37, https://doi.org/10.1016/j.cpc.2016.03.003.

[25] B. Gajdics, J.J. Tomán, Z. Erdélyi, An effective method to calculate atomic movements in 3D objects with tuneable stochasticity (3DO-SKMF), Comput. Phys. Commun. 258 (2021) 107609, https://doi.org/10.1016/j.cpc.2020.107609.

[26] G. Jáger, J.J. Tomán, Z. Erdélyi, Nanoparticle formation by spinodal decomposition in ion implanted samples, J. Alloys Compd. 910 (2022) 164781, https://doi.org/10.1016/j.jallcom.2022.164781.

[27] N.L. Johnson, S. Kotz, N. Balakrishnan, Continuous Univariate Distributions Vol. 2, Wiley-Interscience, 1995.

[28] A.G. Khachaturyan, Theory of Structural Transformations in Solids, Dover Publications, 2013. URL, https://www.ebook.de/de/product/22190925/armen_g_khachaturyan_theory_of_structural_transformations_in_solids.html.

[29] Y. Wang, D. Banerjee, C. Su, A. Khachaturyan, Field kinetic model and computer simulation of precipitation of l12 ordered intermetallics from f.c.c. solid solution, Acta Mater. 46 (9) (1998) 2983–3001, https://doi.org/10.1016/s1359-6454(98)00015-9.

[30] A. Gusak, T. Zaporozhets, Martin's kinetic mean-field model revisited—frequency noise approach versus Monte Carlo, Metallofiz. Noveishie Tekhnol. 40 (11) (2018) 1415–1435, https://doi.org/10.15407/mfint.40.11.1415.

[31] A. Gusak, T. Zaporozhets, N. Storozhuk, Phase competition in solid-state reactive diffusion revisited—stochastic kinetic mean-field approach, J. Chem. Phys. 150 (17) (2019) 174109, https://doi.org/10.1063/1.5086046.

[32] B. Gajdics, J.J. Tomán, Z. Erdélyi, Composition dependent gradient energy coefficient: how the asymmetric miscibility gap affects spinodal decomposition in Ag-Cu? Calphad 67 (2019) 101665 https://doi.org/10.1016/j.calphad.2019.101665.

[33] B. Gajdics, J.J. Tomán, H. Zapolsky, Z. Erdélyi, G. Demange, A multiscale procedure based on the stochastic kinetic mean field and the phase-field models for coarsening, J. Appl. Phys. 126 (6) (2019) 065106, https://doi.org/10.1063/1.5099676.

[34] T.V. Zaporozhets, A. Taranovskyy, G. Jáger, A.M. Gusak, Z. Erdélyi, J.J. Tomán, The effect of introducing stochasticity to kinetic mean-field calculations: comparison with lattice kinetic Monte Carlo in case of regular solid solutions, Comput. Mater. Sci. 171 (2020) 109251, https://doi.org/10.1016/j.commatsci.2019.109251.

[35] A. Taranovskyy, J.J. Tomán, B.D. Gajdics, Z. Erdélyi, 3d phase diagrams and the thermal stability of two-component janus nanoparticles: effects of size, average composition and temperature, Phys. Chem. Chem. Phys. 23 (10) (2021) 6116–6127, https://doi.org/10.1039/d0cp06695h.